Vrije Universiteit Brussel

Series and Parallel Elastic Actuation: Influence of Operating Positions on Design and Control

Beckerle, Philipp; Verstraten, Tom; Mathijssen, Glenn; FURNéMONT, Raphaël Guy; Vanderborght, Bram; Lefeber, Dirk

Series and Parallel Elastic Actuation: Influence of Operating Positions on Design and Control

Philipp Beckerle, *Member, IEEE,* Tom Verstraten, *Student Member, IEEE,* Glenn Mathijssen, *Student Member, IEEE,* Raphaël Furnémont, *Student Member, IEEE,* Bram Vanderborght, *Member, IEEE,* and Dirk Lefeber, *Member, IEEE*

Abstract—It is well-established that properly tuned elastic elements can make robotic actuators more energy-efficient, especially in cyclic tasks. Considering drive train topology, two important subcategories of elastic actuators are Series Elastic Actuation (SEA) or Parallel Elastic Actuation (PEA). There is still no definite answer to the fundamental question which topology consumes less energy in a given task. This paper approaches the problem by studying oscillatory motions of a single degree-of-freedom link in a gravitational field. The imposed motion is a sinusoid with non-zero offset requiring a static torque that needs to be compensated by the actuation system. Simulations and experiments show that SEA consumes less energy up to certain offset angles. At high offsets, PEA becomes the more energy-efficient alternative, provided that its no-load angle is properly tuned. Inverse dynamics simulations show how a threshold offset angle can be determined for a given task.

Index Terms—Compliant actuators, Energy efficiency, Dynamics, Series Elastic Actuators, Parallel Elastic Actuators.

I. Introduction

The development of robotics is heading towards close human-robot interaction which results in a high relevance of soft robot designs [1], [2], [3], [4]. Elastic robots can provide human safety in working environments [1], [3] and be beneficial in motion assistance [5], [6] and rehabilitation [7]. Elastic actuators can furthermore improve robot efficiency by adapting their own characteristics to the operating state [8], [9], [10], e. g., by matching natural system behavior to cyclic trajectories [11]. Various concepts for actuators incorporating fixed or variable elasticity have been proposed [12] of which most comprise a serial elastic element to couple drive and link compliantly for safe human-robot interaction. This concept of Serial Elastic Actuation (SEA) can be implemented with fixed, physically variable, or virtually variable stiffness where the latter two ones rely on either mechanisms or controls. These approaches can be used to dynamically adapt to human-safety or energy efficiency requirements in Variable Stiffness Actuators (VSA) [12], [13], [14].

Characterization and modeling is crucial to take advantage of natural dynamics by design and control. Inertial and gravitational effects have distinct influence on the natural dynamics,

P. Beckerle is with Institute for Mechatronic Systems in Mechanical Engineering, Technische Universität Darmstadt, Otto-Berndt-Straße 2, 64287 Darmstadt, Germany, `beckerle@ims.tu-darmstadt.de`

T. Verstraten, G. Mathijssen, R. Furnémont, B. Vanderborght, and D. Lefeber are with Robotics and Multibody Mechanics Research Group (R&MM), Vrije Universiteit Brussel, Pleinlaan 2, 1050 Elsene, Belgium

and resonance and antiresonance modes can be exploited [11], [15]. Further, the configuration of elastic elements and motors has distinct impact on dynamics and energy efficiency. Besides SEA, Parallel Elastic Actuation (PEA) or concepts combining serial and parallel elastic elements may provide advantageous power and energy characteristics [16], [17], [18]. To cover different operating frequencies in cyclic tasks by stiffness variation, SEA implementations require lower stiffness bandwidths than PEA [11], [19]. Despite the advantages of SEA, it has been shown that various applications can benefit from parallel elements if they are tuned task-specifically, e.g., by pretension [16], [20]. Since robotic workspaces usually cover a range of operating points, understanding their impacts on natural dynamics can help to improve actuator design and control.

This paper compares the natural dynamics and power as well as energy characteristics of PEA and SEA regarding mechanical and electrical dynamics including energy regeneration [21]. Section II describes the models and dynamics of the examined actuators considering the operating position and determines their linearized natural behavior. Nonlinear inverse dynamics analyses of power and energy requirements are presented in Section III to identify the potential of utilizing knowledge about the linearized natural behavior in design and control. Experimental investigations with the test setup from [21] are used to evaluate the analytically obtained results (Section IV). The results are concluded in Section V.

II. Dynamics modeling

The schematic topologies of a PEA and a SEA moving a one degree of freedom pendulum with a mass M and a length l (the distance between turning point and center-of-mass) are shown in Figure 1. The frontal view of the driven pendulum is given in Figure 1 a) and presents the direction of θ, the operating position offset θ_o as well as its maximum and minimum values $\pm\theta_{max}$. Further, the no-load angle θ_{nl} to which the pendulum returns if the elasticity of the PEA is unloaded is given. For both topologies, actuator and gearbox inertia are denoted as J_m and J_{tr}, the gear ratio is n, and motor position is given by θ_m. As can be seen in Figure 1 b), the load inertia of the PEA is $J_l = J_{l1} + J_{l2}$, its stiffness is k_p, and angular positions of the pendulum are equal to those at the gearbox output. The pendulum motions correspond to the reduced motor motions $\theta = n^{-1}\theta_m$ and are caused by the torque T_m. In the SEA with a serial stiffness k_s that is shown in Figure 1 c), inertia J_{1l} and J_{2l} are separated by the elastic element and the positions of pendulum θ and gearbox output $n^{-1}\theta_m$ differ.
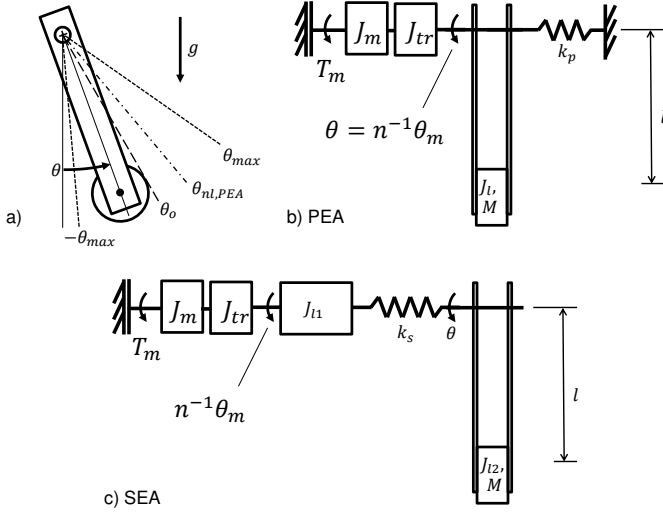
Fig. 1: Pendulum load (top left) and considered actuator topologies (right): a) frontal view, b) Parallel Elastic Actuator, c) Series Elastic Actuator.

A. Parallel Elastic Actuation (PEA)

Literature indicates that the no-load angle θ_{nl} of the parallel spring can be an important design parameter with respect to energy efficiency [20], [16]. Considering this angle in the nonlinear dynamics model according to [21], the required motor torque can be calculated by

$$T_m = J_{mt}n\ddot{\theta} + \frac{C}{n}\left(T_e + k_p\left(\theta - \theta_{nl}\right)\right) \tag{1}$$

in which T_e represents the load torque in the elastic element given by

$$T_e = J_l\ddot{\theta} + T_c\text{sign}\left(\dot{\theta}\right) + \nu\dot{\theta} + Mgl\sin\theta \tag{2}$$

The load includes inertial terms, Coulomb friction, viscous friction and gravitational effects. $J_{mt} = J_m + J_{tr}$ denotes the combined inertia of motor and gearbox. The latter part of (1) is scaled by the gear ratio n and the gearbox efficiency function C:

$$C = \begin{cases} 1/\eta_{tr} & \text{(load driven by motor)} \\ \eta_{tr} & \text{(motor driven by load)} \end{cases} \tag{3}$$

which models the dynamic behavior of a gearbox and takes into account power flow reversal [22]. Linearizing (1) using a Taylor series to analyze the natural dynamics at a certain operating position offset θ_o yields

$$\begin{aligned} \Delta T_m &= J_{mt}n\Delta\ddot{\theta} \\ &+ \frac{C}{n}\left(J_l\Delta\ddot{\theta} + \nu\Delta\dot{\theta} + Mgl\cos\theta_o\Delta\theta + k_p\Delta\theta\right) \end{aligned} \tag{4}$$

which describes small motions $\Delta\theta = \theta - \theta_o$ of the pendulum around this position. Note that this equation corresponds to the one used in [19] if $\theta_o = 0$. It further becomes obvious that the offset angle θ_o does not impact this behavior as well as Coulomb friction which only influences the amplitude.

Neglecting friction and gearbox losses, the single resonance frequency of this second-order system is:

$$\omega_{rs,PEA} = \pm\sqrt{\frac{k_p + Mgl\cos\theta_o}{J_l + n^2 J_{mt}}} \tag{5}$$

Comparing this to the model given in [19] indicates that the operating position offset θ_o does impact the dynamic behavior. A similar influence is found when calculating the resonance frequency of the link only with the torque at the gearbox shaft:

$$\omega_{rl,PEA} = \pm\sqrt{\frac{k_p + Mgl\cos\theta_o}{J_l}} \tag{6}$$

The relevance of this frequency is shown in [19] as the mechanical energy consumption is minimal at the resonance frequency of the link for offset-free sinusoidal motions.

Analyzing the steady state behavior of the PEA can shed light on the influence of the offset angle θ_o. Considering energy consumption, the favorable no-load angle θ_{nl} for this specific position offset is found if no torque is required to hold the static position, i.e., $T_m(\theta_o) = 0$. It can be calculated by substituting the operating position offset θ_o in the static part of (1) [23]:

$$\theta_{nl} = \theta_o + \frac{Mgl\sin\theta_o}{k_p} \tag{7}$$

Here, modeling gives an important design indication since this favorable no-load angle θ_{nl} is not equal to the operating position offset θ_o. Still, it can be calculated analytically without simplifying the nonlinear dynamics of the system. Functionally, this mechanical implementation corresponds to a feed-forward compensation of the gravitational effect. This brings the system to the offset position θ_o in the steady state.

B. Series Elastic Actuation (SEA)

As a result of the decoupling of motor and gearbox inertia, SEAs exhibit fourth-order dynamics as discussed in [11], [19]. This is due to the deformation of the spring, which causes a difference between link and motor position that depends on the load torque T_e given in (2) (compare [19]):

$$\theta_m = n\left(\frac{T_e}{k_s} + \theta\right) \tag{8}$$

Because of the relation between link and motor position, an equilibrium angle as in the PEA case cannot be defined. Thus, the nonlinear equations of motion from [19] apply:

$$\begin{aligned} 0 &= J_{l2}\ddot{\theta} + \nu_{l2}\dot{\theta} + T_{c,l2}\text{sign}(\dot{\theta}) \\ &+ Mgl\sin\theta - k_s\left(\frac{\theta_m}{n} - \theta\right) \end{aligned} \tag{9}$$

$$\begin{aligned} T_m &= (nJ_{mt} + J_{l1})\frac{\ddot{\theta}_m}{n} + \frac{C}{n}\left(k_s\left(\frac{\theta_m}{n} - \theta\right)\right) \\ &+ \frac{C}{n}\left(T_{2c}\text{sign}(\frac{\dot{\theta}_m}{n}) + \nu_2\frac{\dot{\theta}_m}{n}\right) \end{aligned}$$

Here, link dynamics are given by the first equation, while the second refers to the motor dynamics. Note that the calculation of motor torque T_m requires differentiation of (8).

This function is generally discontinuous because of Coulomb friction, leading to the appearance of Dirac pulses in the first derivative. Because such pulses cannot be dealt with in inverse dynamics calculations, the derivatives of Coulomb friction were neglected in the simulations. Linearizing and combining these equations while neglecting friction yields:

$$(nJ_{mt} + J_{l1})\frac{\Delta\ddot{\theta}_m}{n} + \frac{1}{n}\left(J_{l2}\Delta\ddot{\theta} + Mgl\cos\theta_o\Delta\theta\right) = \Delta T_m \tag{10}$$

The natural dynamics are analyzed based on the transfer function found by rewriting (10) as a function of θ_m:

$$H(\omega) = \frac{\Delta\theta_m}{\Delta T_m} = \frac{c_{n2}\omega^2 + c_{n0}}{c_{d4}\omega^4 + c_{d2}\omega^2 + c_{d0}} \tag{11}$$

with the coefficients:

$$\begin{cases} c_{n2} = & -nJ_{l2} \\ c_{n0} = & n\left(Mgl\cos\theta_o + k_s\right) \\ c_{d4} = & (nJ_{mt} + J_{l1})J_{l2} \\ c_{d2} = & -(nJ_{mt} + J_{l1})\left(Mgl\cos\theta_o + k_s\right) - \frac{k_s}{n}J_{l2} \\ c_{d0} = & k_s\frac{1}{n}Mgl\cos\theta_o \end{cases}$$

The zeros of this transfer function determine the antiresonance frequency of the system:

$$\omega_{a,SEA} = \sqrt{\frac{k_s + Mgl\cos\theta_o}{J_{l2}}} \tag{12}$$

Its poles correspond to the two resonance frequencies of the system that are calculated by:

$$\omega_{r1/2,SEA} = \pm\left(\frac{-c_2 \pm \sqrt{c_2^2 - 4c_4c_0}}{2c_4}\right)^{1/2}$$

C. Motor model

A DC motor model is used to calculate load- and speed-dependent motor losses using data sheet specifications according to [21]. The electrical power consumption P_{elec} is calculated as follows:

$$P_{elec} = UI$$

The corresponding voltage U and current I are calculated with the widely adopted DC motor model (see [24]):

$$\begin{cases} I = \frac{T_m + \nu_m\dot{\theta}_m}{k_t} \\ U = L\frac{dI}{dt} + RI + k_b\dot{\theta}_m \end{cases} \tag{13}$$

The parameters R and L denote winding resistance and terminal inductance while k_t and k_b represent the torque and speed constants. All of them are readily available on the datasheets of manufacturers. Losses due to friction of motor bearings and brushes are represented by viscous damping $\nu_m\dot{\theta}_m$. The corresponding coefficient ν_m is usually not specified on datasheets but can be estimated based on the assumption that the consumed current at the no-load speed ω_{nl} exactly equals the no-load current I_{nl}:

$$\nu_m = \frac{k_t \cdot I_{nl}}{\omega_{nl}} \tag{14}$$

TABLE I: Pendulum and gearbox properties

Parameter	Value
Gearbox shaft inertia (J_{l1})	$1.31e - 4\,\mathrm{kgm^2}$
Output shaft inertia (J_{l2})	$1.57e - 1\,\mathrm{kgm^2}$
Mass (M)	$1.85\,\mathrm{kg}$
Distance from rotation axis to COG (l)	$0.241\,\mathrm{m}$
Coulomb friction coefficient ($T_{c,l1}$)	$0.082\,\mathrm{Nm}$
Coulomb friction coefficient ($T_{c,l2}$)	$0.13\,\mathrm{Nm}$
Damping coefficient (ν_{l1})	$0.15\,\mathrm{Nms/rad}$
Damping coefficient (ν_{l2})	$0.045\,\mathrm{Nms/rad}$
Gear ratio (n)	$338/3$
Gearbox inertia (J_{tr})	$5e - 7\,\mathrm{kgm^2}$
Gearbox efficiency (η_{tr})	$72\,\%$

To take the speed- and torque-dependent energy losses of gearboxes into account, the only parameters given by most manufacturers are utilized according to [25], i.e., gearbox inertia J_{tr}, gear ratio n, and maximum gearbox efficiency η_{tr}. The latter two are incorporated into the gearbox efficiency function C defined in (3) according to the approach presented and validated in [25]. The electrical dynamics of the motor are simplified in natural dynamics analysis since the effects induced by its terminal inductance L and winding resistance R are several orders of magnitude smaller than back-EMF $k_b\dot{\theta}_m$ for most operating situations. The transfer behavior between motor voltage and pendulum motion (U/θ) only differs from the one between motor and pendulum motion in gain and by an additional pole at $s = 0$. This indicates that minimum voltage should coincide with antiresonance of the mechanical subsystem. Regarding current, T_m has major impact across most of the operating range and thus the dynamics between motor current and pendulum position are closely related to those of motor torque and pendulum position. This shows that resonance operation yields a current reduction.

III. INVERSE DYNAMICS ANALYSIS

As in [8], [11], [19], PEA and SEA are investigated considering a pendulum setup. Yet, desired motion trajectories are generated to consist of a sinusoidal component that oscillates symmetrically around a particular operating position offset θ_o:

$$\theta = \theta_a\sin(\omega t) + \theta_o \tag{15}$$

Since the amplitude θ_a of this trajectory is $15\,°$ and added to the offset values of $0\,°$ to $25\,°$, the small-angle approximation is not applied but the full nonlinear equations of motion are considered in the simulations. The results from the simulations are obtained from inverse dynamics, assuming perfect tracking of the trajectory at the output. The physical properties given in Table I are chosen according to those of the setup from [19], which is later used for experimental evaluation.

A. Parallel elastic actuation

Figure 2 presents the results obtained by inverse dynamics analysis of mechanical peak power as well as mechanical and electrical energy consumption of PEA. The relations of those quantities to the natural dynamics and no-load angle are indicated by the grey, black, and white lines which represent

system resonance, link resonance, and the offset to which the system is tuned. Globally, mechanical peak power increases with rising frequency and is reduced to about $0.6\,\text{W}$ and $2.8\,\text{W}$ at the resonance frequencies of the system $\omega_{rs,PEA}$ (grey line) and the link $\omega_{rl,PEA}$ (black line), respectively. The equilibrium angle is set to the favorable value of $17.3\,^\circ$ for operation at $10\,^\circ$ which is indicated by the white line. For operation around this favorable value over a large range of frequencies, significant reduction of peak power is observed. Further, a distinct minimum is observed when operating at the favorable offset slightly above the system resonance frequency $\omega_{rs,PEA}$ since the torque of the motor is minimal at this point.

The results for mechanical energy consumption show a very distinct reduction when operating at the favorable equilibrium angle as well. In contrast to mechanical peak power, a minimum occurs near the intersection of the lines representing

operation tuned with respect to the offset and the link resonance frequency $\omega_{rl,PEA}$. The latter is due to the dominance of gearbox losses when considering mechanical energy [19]. The optimum is observed at a frequency of $7.9\,rad/s$, slightly lower than the theoretical resonance frequency of $8.1\,\text{rad/s}$. This is due to friction losses proportional to speed, which tend to lower the optimal frequency [19].

Electrical energy consumption is generally high when not operating at the favorable angle. With respect to the offset, the energy minimum is located around the operating position offset θ_o for which the system is tuned. Regarding frequency, the optimum is found at $7.0\,rad/s$. This is in between the system and link resonances $\omega_{rs,PEA} = 6.0\,\text{rad/s}$ and $\omega_{rs,PEA} = 8.1\,\text{rad/s}$ which is typical for PEA [19]. Compared to the mechanical energy consumption, the minimum of the electrical one is even more pronounced. The area of low
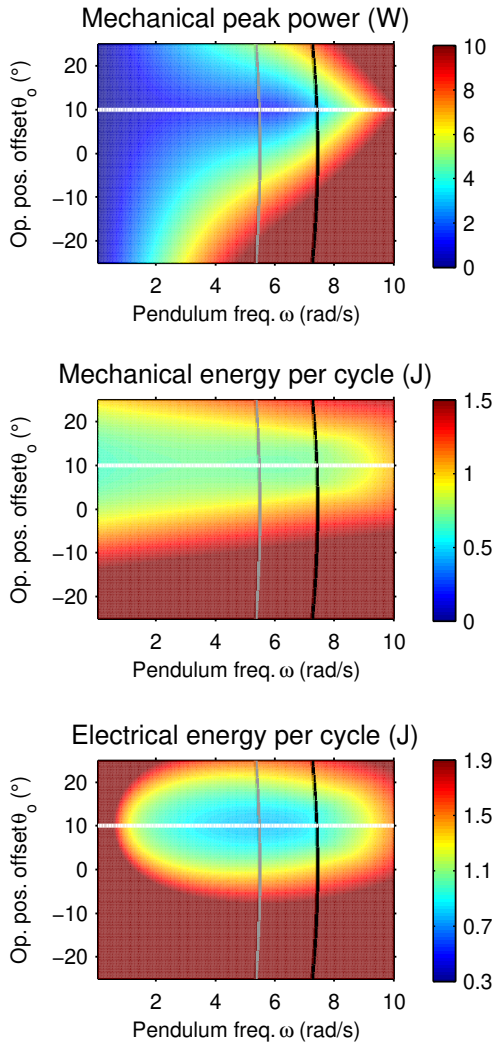

Fig. 2: Mechanical peak power, mechanical, and electrical energy consumption obtained by inverse dynamics calculations of PEA with $k_p = 4.5\,\text{Nm/rad}$. Grey, black, and white lines represent system resonance, link resonance, and the offset to which the system is tuned.
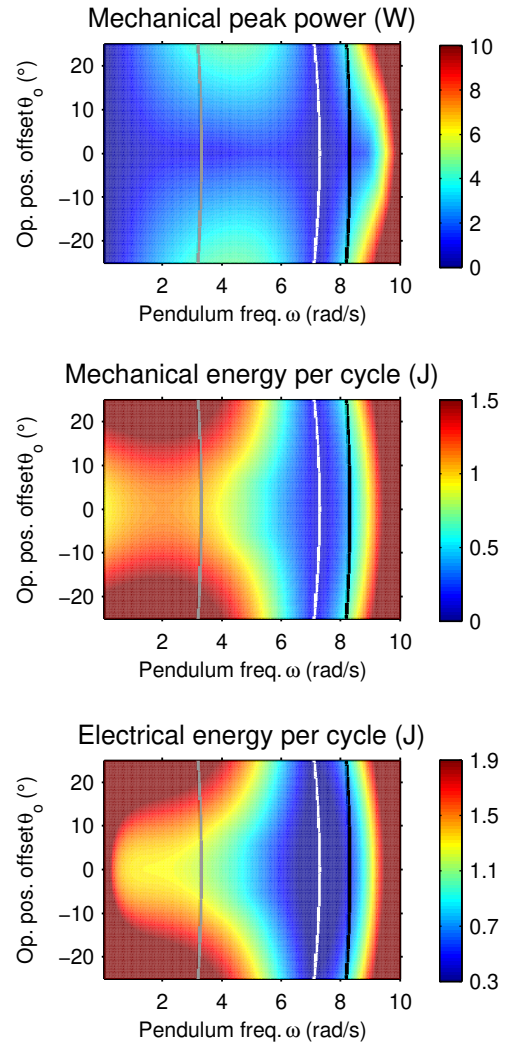
Fig. 3: Mechanical peak power, mechanical, and electrical energy consumption obtained by inverse dynamics calculations of SEA with $k_s = 4\,\text{Nm/rad}$. Grey, black, and white lines represent first resonance and second resonance as well as antiresonance.

energy consumption due to adjustment of the no-load angle θ_{nl} covers a wide range of frequencies. Hence, this parameter seems to be an important tool to cancel out the static torque caused by the operating position offset. The tuning of the PEA can further be extended by changing the stiffness of the elastic element, as studied in [19].

B. Series elastic actuation

The mechanical peak power as well as the mechanical and electrical energy consumption found for SEA are presented in Figure 3. A distinct minimum of the mechanical peak power is found at antiresonance frequency $\omega_{a,SEA}$ (white line) that is warped by the influence of the operating position offset. For higher offsets, the analytically predicted curvature of antiresonance is more distinct than that of the power minimum in the simulations (between 7.3 and 7.1 rad/s). This is caused by the relatively high value of the offset compared to the amplitude of the movement and the fact that the small angle approximation loses accuracy. However, the minimum can roughly be predicted analytically using linear models. Generally, mechanical power is rather low if $\theta_o = 0$ rad since SEAs do not exhibit equilibrium angles and return to $\theta = 0$ rad when unloaded. At non-zero offsets, a static torque is required. Since this torque cannot be delivered by the series spring, energy consumption increases.

A less distinct minimum is found around zero offset and 3.7 rad/s which is close to the first resonance $\omega_{r1,SEA}$ (grey line). The second resonance $\omega_{r2,SEA}$ (black line) does not lead to any observable minimum. Consequently, power requirements rise monotonically with increasing frequency beyond antiresonance [19].

Mechanical energy consumption shows a minimum at antiresonance $\omega_{a,SEA}$ that is even more pronounced than in mechanical peak power. It resembles the analytically determined lines almost perfectly. As in [19], no minima are observed at first resonance $\omega_{r1,SEA}$ and second resonance $\omega_{r2,SEA}$ since the gear box speed is minimal at antiresonance while gear box torque is minimal close to the link resonance of the rigid system (which corresponds to $\omega_{rl,PEA}$ for $k_p = 0$ Nm/rad). As for mechanical power, reduced energy consumption is found around zero offset due to the non-existence of an equilibrium position in the SEA case. As for mechanical power, reduced energy consumption is found around zero offset because the SEA cannot compensate for a static torque.

The electrical energy consumption shows the same trends as the mechanical one. Energy consumption is minimal around antiresonance $\omega_{a,SEA}$ and at low offsets θ_o. Comparing Figure 2 and Figure 3 shows that the energy requirements of the SEA at antiresonance are still lower than those of the PEA within the investigated offset range even if the latter is tuned with respect to the offset. Yet, the minimum energy consumption area of the offset-adjusted PEA covers a certain frequency range. For SEA, energy consumption is more sensitive to frequency variation and hence stiffness variation might be important for certain applications. In contrast, the PEA might not require stiffness tuning for tasks with a fixed offset and a limited frequency range. However, both effects
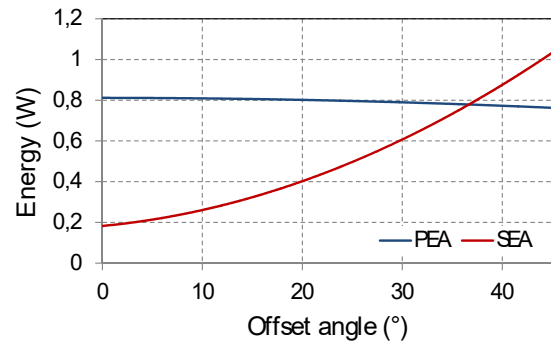

Fig. 4: Investigation of offset effects on electrical energy consumption of PEA and SEA. PEA is tuned with respect to the offset angle and system resonance $\omega_{rs,PEA}$ while SEA is operating at antiresonance $\omega_{a,SEA}$.

depend on the value of the offset which is investigated in detail further ahead.

C. Effects of arbitrary offsets

As shown above, antiresonance-adjusted SEA can outperform PEA regarding electrical energy consumption in the investigated offset range even if the PEA is tuned by setting the no-load angle to the optimal value. To find out whether this is a general effect or the advantage of SEA disappears for larger offsets, energy consumption is calculated for offsets of $0°$, $15°$, $30°$, and $45°$. Within this, PEA and SEA operate at their optimal operating points, i.e, stiffness is tuned to the system resonance $\omega_{rs,PEA}$ (PEA) or antiresonance $\omega_{a,SEA}$ (SEA), and the no-load angle of PEA is set according to (7). The curves of the minimum electrical energy consumptions depending on the offset are fitted using second order polynomials and given in Figure 4. SEA performs better for low offsets while PEA is beneficial for trajectories with offsets higher than $36°$. This is due to the static gravitational torque that can be compensated by changing the no-load angle of the spring. It has to be noted that PEA consumption is slightly overestimated since its real optimum would be found below system resonance as described in Section III-A. Nevertheless, the advantages of PEA at higher offsets are obvious.

IV. EXPERIMENTAL EVALUATION

To evaluate the insights regarding power and energy, electrical energy consumption is experimentally measured with the setup from [19] which shows the same parameters as used for the inverse dynamics calculations. It is driven by 80 W Maxon DCX35L motor through Maxon GPX42 338 : 3 planetary gearbox. The rotationally compliant elements are realized by pairs of antagonistic tension springs connected by wires as shown in Figure 5. The springs are exchanged to modify actuator stiffness in discrete steps between the experimental trials. The resulting rotational stiffness values can be varied between 0.3 Nm/rad and 2.3 Nm/rad for the PEA as well as 2 Nm/rad and 10 Nm/rad for the SEA.

For the acquisition of mechanical energy consumption, a torque sensor and an optical position encoder measure the

Fig. 5: Experimental setup: PEA (left) and SEA (right) configuration. Gearbox and output shaft are equipped with incremental encoders. Additionally, a torque sensor is included at the gearbox output. The length of the drive train, output shaft, and pendulum are $0.44[m]$, $0.27[m]$, and $0.40[m]$, respectively.

quantities on the gearbox shaft. Another optical encoder senses the output shaft angle of the SEA. For the assessment of electrical energy consumption, motor voltage and current are acquired. All sensors are considered in the system model according to [19] to ensure a sound comparison of simulations and experiments. In the experiments, sensor data is acquired with a National Instruments sbRIO 9626 board that also runs the control algorithms. Mechanical power is calculated from torque measurements from an ETH Messtechnik DRBK-I torque sensor (max. error $0.1\,\mathrm{Nm}$) and speed obtained from a US Digital E6 optical encoder (resolution 2000 counts per turn). Electrical power values are acquired by multiplying battery voltage and current which is measured by an Allegro ACS712 current sensor (max. error 1.5%). The desired trajectory is generated by a Maxon EPOS2 50/5 motor controller powered by two $12\,\mathrm{V}$ lead-acid batteries placed in series.

For every combination of actuator stiffness and trajectory frequency, at least ten pendulum periods were recorded after start-up transients had settled, i.e., the first five to ten oscillations are not taken into account. The considered ones are decomposed into separate sine periods which are averaged to reduce non-reproducible effects such as noise.

A. Control algorithm

Feedback linearization is chosen to control the nonlinear dynamics of both configurations [23] and tackle the missing collocation due to the elastic coupling of the SEA [26]. For PEA and SEA, the nonlinear dynamics are compensated through applying an appropriate motor current. For PEA, this is

$$I_{m,PEA} = \frac{1}{k_t}\left[\left(nJ_{mt}+\frac{J_l}{n}\right)y_{PEA}\right] \tag{16}$$
$$+ \frac{1}{k_t}\left[\frac{Mgl}{n}\sin(\theta)+\frac{k_p}{n}(\theta-\theta_{nl})\right]$$

Denoting driveside inertia by $J_{dr}=nJ_{mt}+J_{l1}$ the equation

for SEA is:

$$I_{m,SEA} = \frac{1}{nk_t}\left(J_{l2}\ddot{\theta}+Mgl\sin\theta\right) \tag{17}$$
$$+ \frac{J_{dr}}{k_t}\left(\frac{J_{l2}y_{SEA}+Mgl(\cos\theta\ddot{\theta}-\sin\theta\dot{\theta}^2)}{k_s}+\ddot{\theta}\right)$$

Both control laws combine feedback motion control by the auxiliary input y_{PEA} or y_{SEA} with a feed-forward term that is based on (1) or (10), respectively. The auxiliary control inputs are designed as suggested in [23]:

$$y_{PEA/SEA} = \overset{....}{\theta}_d + R_0(\theta_d-\theta)+R_1\left(\dot{\theta}_d-\dot{\theta}\right) \tag{18}$$
$$+ R_2\left(\ddot{\theta}_d-\ddot{\theta}\right)+R_3\left(\dddot{\theta}_d-\dddot{\theta}\right)$$

where $\ddot{\theta}_d$, $\dot{\theta}_d$, θ_d are the desired angular accelerations, velocities, and positions of the pendulum. The control parameters R_0 and R_1 are used to design a proportional and differential controller that commands the second-order dynamics of the PEA while for the SEA all four parameters are utilized due to its fourth-order behavior [27]. For both, the parameters are manually tuned for each investigated combination of frequency and stiffness to ensure the best possible tracking for a sound comparison of power and energy characteristics.

As controller inputs, the first three derivatives of the output position signal are required. To avoid numerical issues, the second and third derivative are calculated by means of the state vector $\begin{bmatrix}\theta\,\theta_m\,\dot{\theta}\,\dot{\theta}_m\end{bmatrix}^T$ using a first-order differentiator (resolution $1000\,\mathrm{cpt}$ and sampling time $2000\,\mathrm{Hz}$. As shown in [21], the controller has a negligible influence on power and energy consumption, provided that the output trajectory is tracked well.

B. Experimental results

The experimentally obtained electrical energy consumption data are presented in Figure 6 for the PEA and in Figure 7 the SEA. For PEA, the experimental results (green circles) are in good accordance with those from simulation (blue grid). The experiments confirm that lowest energy consumptions
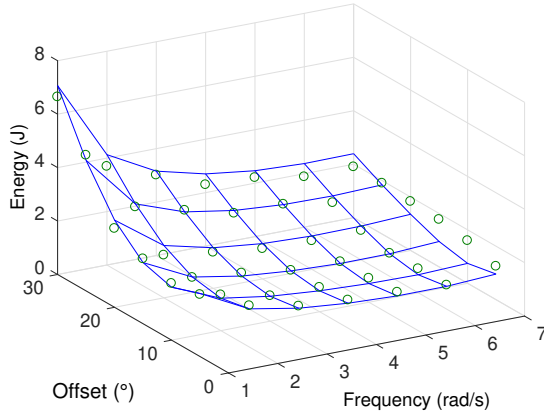
Fig. 6: Electrical energy consumption of PEA: comparison of analytical calculations (blue grid) and experiments (green circles).

Fig. 7: Electrical energy consumption of SEA: comparison of analytical calculations (blue grid) and experiments (green circles).

occur at an offset of $\theta_o = 10°$ for which the actuator was tuned. Global minima of $0.89\,\mathrm{J}$ ($\omega = 5\,\mathrm{rad/s}$, $\theta_o = 10°$) and $0.86\,\mathrm{J}$ ($\omega = 6\,\mathrm{rad/s}$, $\theta_o = 15°$) are found in the experiment. If measurements would be taken continuously and not in a discrete grid, the actual optimum would have been found between those frequencies as discussed in Section III-A, i.e., slightly below the intersection of the optimal offset and system resonance $\omega_{rs,PEA} = 5.6\,\mathrm{rad/s}$. Obviously, energy consumption is on a rather low level in the proximity of the measured minima and thus their accuracy and comparison might distinctly be affected by experimental deviations. Still, the experiment demonstrates that the analytic expression (7) can be used to adapt the no-load angle of a PEA to the trajectory offset. During the trials at $7\,\mathrm{rad/s}$, one of the cables was observed to sag due to the highly dynamic loads. For this reason, the results at this frequency are not entirely reliable which may explain their deviation from the calculated values.

Considering the results for the SEA shown in Figure 7, the measurements match the simulations similarly well as for PEA. An area of low energy consumption is found at offsets of $\theta_o = 0°$ confirming the simulation results. The global energy consumption minimum of $0.25\,\mathrm{J}$ is found at $7\,\mathrm{rad/s}$ and $0°$. The frequency of $7\,\mathrm{rad/s}$ roughly corresponds to the theoretical antiresonance frequency $\omega_{a,SEA} = 7.4\,\mathrm{rad/s}$, which is the energy-optimal operating point for the SEA [19].

Figure 6 and Figure 7 demonstrate that the minimum of the SEA ($0.24\,\mathrm{J}$) is lower than that of the PEA ($0.9\,\mathrm{J}$). This confirms the analytical finding of lower energy consumption in an antiresonance-tuned SEA. However, this advantage of the SEA should disappear at higher offsets as shown in the simulation in Section III.

V. Conclusion

This paper investigates the influence of oscillatory motions with differing operating positions on the power and energy consumption of elastic actuators. By investigating and comparing the characteristics of Parallel and Serial Elastic
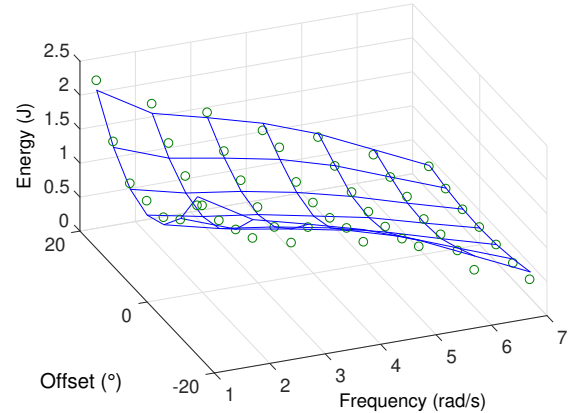
Actuators (PEA and SEA), implications for design and control are determined.

Intuitively, one might expect a PEA to show lower energy consumption if tuned with respect to equilibrium position and thus compensating for static loads. Yet, antiresonance-tuned SEAs show the best performance for low offsets when considering electrical energy consumption. This is because SEA function can be interpreted constantly changing the equilibrium position of a spring by the motor to compensate for slight changes in offset. The advantages of SEAs are distinct at low offsets but disappear at higher offsets. A PEA with resonance- and offset-tuning shows roughly constant energy consumption for offsets between $0°$ and $45°$ while the requirements of an antiresonance-tuned SEA would increase with the offset value. Considering inverse dynamics simulations of the investigated system, its specific threshold offset angle is found at about $36°$. In the same way the characteristic offset thresholds can be found for arbitrary systems. By adjusting the corresponding no-load angle, the PEA can further provide rather low energy consumption across a wide range of frequencies if operated at this particular angle.

While the simulations and experiments are performed considering a simple case study, the results concerning the impact of operating position impact are highly relevant for design and control of elastic actuators. They provide a guideline for the selection of an elastic actuator topology considering the particular load, especially with respect to the fraction of static loads. Furthermore, they give insight into the setting of spring stiffness and, in the PEA case, no-load angle. The results demonstrate the capability of PEAs to exploit natural behavior and to bear static loads with very low power consumption. Future work should consider more complex trajectories as well as systems with more sophisticated kinematics and dynamics.

REFERENCES

[1] S. Haddadin, A. Albu-Schaeffer, A. De Luca, and G. Hirzinger, "Collision detection and reaction: A contribution to safe physical human-robot interaction," in *IEEE/RSJ International Conference on Intelligent Robots and Systems*, 2008.

[2] J.-J. Park, Y.-J. Lee, J.-B. Song, and H.-S. Kim, "Safe joint mechanism based on nonlinear stiffness for safe human-robot collision," in *IEEE International Conference on Robotics and Automation*, May 2008, pp. 2177–2182.

[3] T. Lens and O. von Stryk, "Investigation of safety in human-robot-interaction for a series elastic, tendon-driven robot arm," in *IEEE/RSJ International Conference on Intelligent Robots and Systems*, Oct 2012, pp. 4309–4314.

[4] A. Verl, A. Albu-Schaeffer, O. Brock, and A. Raatz, Eds., *Soft Robotics - Transferring Theory to Application*. Springer, 2015.

[5] M. A. Holgate, J. K. Hitt, R. D. Bellman, T. G. Sugar, and K. W. Hollander, "The SPARKy (Spring Ankle with Regenerative Kinetics) project: Choosing a DC motor based actuation method," in *IEEE International Conference on Biomedical Robotics and Biomechatronics*. IEEE, 2008, pp. 163–168.

[6] S. K. Au, J. Weber, and H. Herr, "Powered ankle–foot prosthesis improves walking metabolic economy," *Robotics, IEEE Transactions on*, vol. 25, no. 1, pp. 51–66, Feb 2009.

[7] J. F. Veneman, R. Kruidhof, E. E. G. Hekman, R. Ekkelenkamp, E. H. F. van Asseldonk, and H. van der Kooij, "Design and Evaluation of the LOPES Exoskeleton Robot for Interactive Gait Rehabilitation," *IEEE Transactions on Neural Systems and Rehabilitation Engineering*, vol. 15 (3), pp. 379 – 386, 2007.

[8] B. Vanderborght, R. Van Ham, D. Lefeber, T. G. Sugar, and K. W. Hollander, "Comparison of mechanical design and energy consumption of adaptable, passive-compliant actuators," *The International Journal of Robotics Research*, vol. 28, no. 1, pp. 90–103, 2009.

[9] A. Velasco, M. Garabini, M. G. Catalano, and A. Bicchi, "Soft actuation in cyclic motions: Stiffness profile optimization for energy efficiency," in *IEEE International Conference on Humanoid Robots*, 2015.

[10] A. Jafari, N. Tsagarakis, and D. G. Caldwell, "Energy efficient actuators with adjustable stiffness: a review on AwAS, AwAS-II and CompACT VSA changing stiffness based on lever mechanism," *Industrial Robot: An International Journal*, vol. 42 (3), 2015.

[11] P. Beckerle, J. Wojtusch, S. Rinderknecht, and O. von Stryk, "Analysis of system dynamic influences in robotic actuators with variable stiffness," *Smart Structures and Systems*, vol. 13, no. 4, pp. 711–730, 2014.

[12] B. Vanderborght, A. Albu-Schaeffer, A. Bicchi, E. Burdet, D. Caldwell, R. Carloni, M. Catalano, O. Eiberger, W. Friedl, G. Ganesh, M. Garabini, M. Grebenstein, G. Grioli, S. Haddadin, H. Hoppner, A. Jafari, M. Laffranchi, D. Lefeber, F. Petit, S. Stramigioli, N. Tsagarakis, M. V. Damme, R. V. Ham, L. Visser, and S. Wolf, "Variable impedance actuators: A review," *Robotics and Autonomous Systems*, vol. 61, no. 12, pp. 1601 – 1614, 2013.

[13] G. A. Pratt and M. M. Williamson, "Series elastic actuators," in *IEEE/RSJ International Conference on Intelligent Robots and Systems*, vol. 1, 1995, pp. 399–406 vol.1.

[14] T. Morita and S. Sugano, "Design and development of a new robot joint using a mechanical impedance adjuster," in *IEEE International Conference on Robotics and Automation*, vol. 3, May 1995, pp. 2469–2475 vol.3.

[15] P. Beckerle, J. Wojtusch, J. Schuy, B. Strah, S. Rinderknecht, and O. von Stryk, "Power-optimized stiffness and nonlinear position control of an actuator with variable torsion stiffness," in *IEEE/ASME International Conference on Advanced Intelligent Mechatronics*, July 2013, pp. 387–392.

[16] U. Mettin, P. X. La Hera, L. B. Freidovich, and A. S. Shiriaev, "Parallel elastic actuators as a control tool for preplanned trajectories of underactuated mechanical systems," *The International Journal of Robotics Research*, vol. 29, no. 9, pp. 1186–1198, 2010.

[17] M. Plooij and M. Wisse, "A novel spring mechanism to reduce energy consumption of robotic arms," in *IEEE/RSJ International Conference on Intelligent Robots and Systems*, Oct 2012, pp. 2901–2908.

[18] G. Mathijssen, D. Lefeber, and B. Vanderborght, "Variable Recruitment of Parallel Elastic Elements: Series Parallel Elastic Actuators (SPEA) With Dephased Mutilated Gears," *Mechatronics, IEEE/ASME Transactions on*, vol. 20, no. 2, pp. 594–602, April 2015.

[19] T. Verstraten, P. Beckerle, R. Furnémont, G. Mathijssen, B. Vanderborght, and D. Lefeber, "Series and parallel elastic actuation: Impact of natural dynamics on power and energy consumption," *Mechanism and Machine Theory*, 2016.

[20] M. Grimmer, M. Eslamy, S. Gliech, and A. Seyfarth, "A comparison of parallel- and series elastic elements in an actuator for mimicking human ankle joint in walking and running," in *IEEE International Conference on Robotics and Automation*, May 2012, pp. 2463–2470.

[21] T. Verstraten, G. Mathijssen, R. Furnémont, B. Vanderborght, and D. Lefeber, "Modeling and design of geared DC motors for energy efficiency: Comparison between theory and experiments," *Mechatronics*, vol. 30, pp. 198 – 213, 2015.

[22] H. Giberti, S. Cinquemani, and G. Legnani, "Effects of transmission mechanical characteristics on the choice of a motor-reducer," *Mechatronics*, vol. 20, no. 5, pp. 604 – 610, 2010.

[23] J.-J. E. Slotine, W. Li *et al.*, *Applied nonlinear control*. Prentice-Hall Englewood Cliffs, NJ, 1991, vol. 199, no. 1.

[24] R. Krishnan, *Electric motor ddrive: modeling, analysis, and control*. Prentice-Hall, 2001.

[25] T. Verstraten, R. Furnémont, G. Mathijssen, B. Vanderborght, and D. Lefeber, "Energy consumption of geared DC motors in dynamic applications: Comparing modeling approaches," *IEEE Robotics and Automation Letters (RA-L)*, 2016.

[26] P. Erler, P. Beckerle, B. Strah, and S. Rinderknecht, "Experimental comparison of nonlinear motion control methods for a variable stiffness actuator," in *IEEE International Conference on Biomedical Robotics and Biomechatronics*, Aug 2014, pp. 1045–1050.

[27] B. Siciliano and O. Khatib, *Springer handbook of robotics*. Springer Science & Business Media, 2008.